



CHORUS

This is the accepted manuscript made available via CHORUS. The article has been published as:



Structural tunability and origin of two-level systems in amorphous silicon

H. C. Jacks, M. Molina-Ruiz, M. H. Weber, J. J. Maldonis, P. M. Voyles, M. R. Abernathy, T. H. Metcalf, X. Liu, and F. Hellman

Phys. Rev. Materials **6**, 045604 — Published 25 April 2022

DOI: [10.1103/PhysRevMaterials.6.045604](https://doi.org/10.1103/PhysRevMaterials.6.045604)


Structural tunability and origin of two-level systems in amorphous silicon

H. C. Jacks * and M. Molina-Ruiz  †




Physics Department, University of California, Berkeley, California 94720, USA

M. H. Weber 

Physics and Astronomy Department, Washington State University, Pullman, Washington 99164, USA

J. J. Maldonis  and P. M. Voyles 

Materials Science and Engineering Department, University of Wisconsin - Madison, Wisconsin 53706, USA

M. R. Abernathy , ‡ T. H. Metcalf , and X. Liu 

Naval Research Laboratory, Washington, DC 20375, USA

F. Hellman 

*Physics Department, University of California, Berkeley, California 94720, USA and
Lawrence Berkeley National Laboratory, Berkeley, California 94720, USA*

(Dated: February 28, 2022)

Amorphous silicon films prepared by electron beam evaporation have systematically and substantially greater atomic density for higher thickness, higher growth temperature, and slower deposition rate, reaching the density of crystalline Si when films of thickness greater than ~ 300 nm are grown at 425 °C and at < 1 Å/sec. A combination of spectroscopic techniques provide insight into atomic disorder, local strains, dangling bonds, and nanovoids. Electron diffraction shows that the short-range order of the amorphous silicon is similar at all growth temperatures, but fluctuation electron microscopy shows that films grown above room-temperature show a form of medium-range order not previously observed in amorphous silicon. Atomic disorder and local strain obtained from Raman spectroscopy reduce with increasing growth temperature and show a non-monotonic dependence on thickness. Dangling bond density decreases with increasing growth temperature and is only mildly dependent on thickness. Positron annihilation Doppler broadening spectroscopy and electron energy loss spectroscopy show that nanovoids, and not density variations within the network, are responsible for reduced atomic density. Specific heat and mechanical loss measurements, which quantify the density of tunneling two-level systems, in combination with the structural data, suggest that two-level systems in amorphous silicon films are associated with nanovoids and their surroundings; which are in essence loosely bonded regions where atoms are less constrained.

PACS numbers: 61.43.Dq, 68.37.-d, 78.66.Jg

I. INTRODUCTION

Amorphous silicon is used in photovoltaic, thin-film transistor, quantum computing and gravitational-wave detection technologies [1–5], to name a few, since it is much easier to implement than its crystalline counterpart. The performance of amorphous silicon in these technologies is dependent on its properties, which change with the material structure obtained during the preparation process, or by the addition of other elements, such as hydrogen, that improves the electronic properties. Amorphous silicon (*a*-Si) is typically found 4-fold coordinated, with little variability in bond length, but variability in bond angle and occasional 3-fold coordination leading to dangling bonds. 5-fold coordinated atoms are found in the liquid phase, but not identified in the solid phase [6, 7]. This limited flexibility in solid phase makes it more controllable than systems with highly variable coordination, e.g., amorphous carbon, or multiatomic materials. Four-fold coordination yields an over-constrained atomic environment, which was postulated by Phillips in 1972 to suppress tunneling two-level systems (TLSs) [8], later confirmed by our work on *a*-Si [9–12].

The suppression of TLSs has been of interest to the glass community because they are the source of energy loss at low temperatures and the origin of anomalous acoustic, thermal, and dielectric properties [13]. The ability to control the TLS density in glasses is crucial in applications for which *a*-Si is a potential material, including phase-resonant

* Present address: Physics Department, California Polytechnic University, San Luis Obispo, California 93407, USA.

† Corresponding author: manelmolinaruiz@gmail.com; H. C. Jacks and M. Molina-Ruiz contributed equally to this work.

‡ Present address: Johns Hopkins University Applied Physics Laboratory, Laurel, Maryland 20723, USA.

qubits [14–16] and coatings for gravitational-waves detection [17, 18]. Electron-beam (e-beam) evaporated *a*-Si shows very low TLS density in high atomic density films, as opposed to high TLS density found in low atomic density films, suggesting that low-density regions are the source of TLSs in e-beam prepared *a*-Si [10–12]. Therefore, a careful understanding of the structural differences between these films should lead to a deeper knowledge of the nature of the TLSs. It has been shown that coupled dangling bonds create tunneling states on the surface of hydrogen terminated crystalline silicon [19], but no correlation between dangling bond density and TLS density has been seen in *a*-Si films [12].

In this work we present extensive structural characterization of *a*-Si films prepared by e-beam evaporation under ultra-high vacuum (UHV) conditions, and show how differences in growth temperature, deposition rate, and film thickness affect the growth mechanisms and film properties. We discuss connections between growth parameters and physical properties, as well as between TLS density and structural features. We conclude that nanovoids are the most likely structures responsible for TLSs in e-beam evaporated *a*-Si films.

II. SAMPLE PREPARATION AND CHARACTERIZATION METHODS

Samples were grown by e-beam physical-vapor deposition (PVD) in an UHV chamber with a base pressure $< 5 \times 10^{-9}$ Torr, and substrate temperature T_S ranging from 50 to 450 °C, growth rate r_t from 0.5 to 2.5 Å/s, and thickness t from 10 to 750 nm. Samples were grown either onto low-stress amorphous silicon nitride (*a*-SiN_x), or onto crystalline silicon with the native oxide layer left intact. A naturally occurring and continuous self-passivating native oxide layer, not thicker than 3 nm [20], was allowed to form on the surface of most *a*-Si films. In some cases, a thin capping layer of Al was used, which forms an excellent passivating layer on exposure to air that protects the film against oxygen and water subsequent to growth.

Structural characterizations, detailed below, span length scales from approximately 0.1 nm to 10 nm. These techniques provide information on both the network and structural defects of the films, specifically surface topography via atomic force microscopy (AFM), atomic density via Rutherford backscattering spectrometry (RBS) together with profilometry and AFM, short-range order (SRO) and medium-range order (MRO) via electron microscopy, atomic bond angle deviation and local strain via Raman spectroscopy, dangling bond density via electron paramagnetic resonance (EPR), and empty space or nanovoids volume via positron annihilation Doppler broadening spectroscopy (DBS) measurements. RBS was also used to set limits on impurities concentration. Elastic recoil detection analysis (ERDA) was used to quantify the films’ water concentration.

With the aim of looking for depth dependence of atomic density and bond angle deviation, and in particular to investigate the origin of the differences seen in properties of thin and thick films [10, 12], select thick films were etched in order to study structural properties as a function of depth. Films were wet etched to avoid densification or atomic reconstruction via energy transfer, since a dry etch may alter the samples underlying atomic structure [21]. To improve thickness control and homogeneity, samples were etched under mild sonication in an isopropanol-saturated 6M KOH bath at 80 °C for several minutes until specific target thicknesses were reached [22].

A. Atomic force microscopy and substrate curvature

A Digital Instruments AFM Nanoscope Dimension 3100 equipped with Budget Sensors Tap300-G silicon probes with a resonant frequency of 300 kHz and force constant of 40 N/m was used to characterize the samples’ surface roughness. The scanned areas are $1 \times 1 \mu\text{m}^2$ yielding root mean square (RMS) surface roughness R_q and topography of the *a*-Si films, as well as of their substrates.

Substrate curvature measurements were taken using a Tencor FLX-2320 thin-film stress measurement instrument. The stress of *a*-Si films grown on 2-in diameter silicon wafers was determined at room-temperature using Stoney’s equation [23] with no corrections, since the thicknesses ratio between films and substrate ($\sim 10^{-4}$) fulfils the condition $\ll 1$ [24].

B. Ion beam analysis and profilometry

The measured atomic density n_{at} of the *a*-Si films is the combined result of profilometry, RBS and AFM measurements. Profilometry was done using a KLA Tencor ASIQ profilometer, with an error between 0.1% to 4% for the thicker and thinner films, respectively. Ion beam analysis was performed by RBS and ERDA in an NEC model 5SDH Pelletron tandem accelerator, with α particles beam energy of 3040 keV. Resonant RBS and ERDA techniques were used to quantify the films’ oxygen and hydrogen content (with detection thresholds of 0.5 at.% O and 0.1 at.% H).

78 RBS was also used to quantify the presence of other impurities. SIMNRA analysis software was used to obtain the
 79 samples composition and areal density [25]. The thickness obtained by profilometry was corrected by the roughness
 80 measured by AFM in order to accurately determine the films' volume. Although the roughness was small (less than
 81 2 nm even in the roughest films), this correction is very important for thinner films.

82 C. Electron microscopy

83 Electron nanodiffraction and electron energy loss spectroscopy (EELS) experiments were performed in a Ther-
 84 moFisher Titan scanning transmission electron microscope (STEM) operated at 200 kV. The diffracted electron
 85 intensity I as a function of the scattering vector \mathbf{k} was measured using energy-filtered electron diffraction on a GIF
 86 865ER with a Gatan US1000 CCD camera at a camera length of 840 mm, an energy filtering with a slit width of 20
 87 eV, and a high coherence, 2 nm diameter nanoprobe beam with a 0.6 mrad semi-convergence angle. One hundred
 88 512×512 pixels nanodiffraction patterns were acquired in a 10×10 grid of positions r covering a 25×25 nm² area
 89 from ten different regions of each sample. The acquisition time for each diffraction pattern was 6 seconds. Each
 90 diffraction pattern was averaged over the azimuthal angle to produce the intensity as a function of the scattering
 91 vector magnitude k .

92 The nanodiffraction data set was used to evaluate short- and medium-range order. SRO was evaluated from $I(k)$,
 93 which is the average of $I(k, r)$ over r . This experiment is the equivalent of a large-area diffraction experiment, but
 94 with somewhat worse k resolution due to the convergent probe. MRO was evaluated using the fluctuation electron
 95 microscopy (FEM) normalized variance V , defined as

$$V(k) = \frac{\langle I^2(k, r) \rangle}{\langle I(k, r) \rangle^2} - 1 \quad (1)$$

96 where values within $\langle \rangle$ are averaged over the position r on the sample. V measures the magnitude of spatial fluctuations
 97 in the diffracted intensity, which are sensitive to three and four-body correlation functions [26–29]. In *a*-Si, MRO spans
 98 length scales from approximately the fourth coordination shell (~ 0.8 nm) to just under what is detectable by Bragg
 99 diffraction (~ 3 nm) [30]. The position in k of peaks in V is controlled by the interatomic spacing inside nanoscale
 100 structural heterogeneities (such as deviations in the distribution of ring sizes, see Ref. 31), and the magnitude of V
 101 is controlled by the size, density, and internal order of the heterogeneities. V was corrected for Poisson noise in I as
 102 described in [27].

103 EELS was performed at a camera length of 160 mm, a probe convergence angle of 25 mrad, and an EELS collection
 104 angle of 52 mrad. The energy dispersion was 0.05 eV/channel, and the energy resolution was 0.8 eV, measured as
 105 the full width at half maximum (FWHM) of the zero-loss peak. EELS experiments focused on the bulk plasmon
 106 loss, which is sensitive to the volume number density of electrons in the material, n . In the Drude model, the peak
 107 plasmon energy $\lambda_0 = \hbar\sqrt{ne^2/\epsilon_0 m}$, where e is the electron charge, m is the electron mass, and ϵ_0 is the permittivity
 108 of free space. At constant composition, shifts in n result from shifts in the volume number density of atoms ρ , which
 109 has been used, for example, to measure thermal expansion in Al as a means of thermometry [32] and the change in
 110 volume of Al on melting [33]. Introducing voids into the sample does not shift λ_0 . Instead, it introduces new plasmon
 111 modes at different energies associated with the surfaces of the voids. As a result, EELS measurements of λ_0 report
 112 the average density of the sample excluding voids, unlike density measurements by RBS or Archimedes principle, and
 113 hence report the average interatomic spacing of the material network.

114 High resolution transmission electron microscopy (HRTEM) was performed on a FEI Tecnai-TF30 microscope
 115 operated at 300 kV. Images with resolution 2048×2048 pixels were recorded by a Gatan Ultrascan CCD with 1
 116 second exposure time. *a*-Si films for all TEM experiments were ~ 30 nm thick grown at different temperatures on
 117 50×50 μm^2 *a*-SiN_x membranes 50 nm thick and measured in plan view.

118 D. Raman spectroscopy

119 The distribution of atomic bonds, or bond angle deviation, $\Delta\theta$ and the fractional volume change, or local strain,
 120 $tr(\epsilon)$ were determined by Raman spectroscopy performed using an inVia Renishaw micro-Raman/PL system equipped
 121 with a 488 nm laser. The laser power was set to ~ 250 μW on a spot with area of ~ 2 μm^2 , low enough to prevent
 122 degradation or crystallization of the amorphous films. Under these conditions, most of the Raman signal comes from
 123 the top ~ 30 nm of the film due to the laser intensity attenuation.

124 In *a*-Si the bond angles have a variability around the tetrahedral angle of 109.5° , the canonical tetrahedral angle in
 125 crystalline silicon (*c*-Si), characterized by $\Delta\theta$. Beeman et al. [34], and later confirmed by others [35, 36], established

126 an empirical correlation between $\Delta\theta$ and the FWHM of the *a*-Si transverse optical (TO) peak, observed at ~ 480
 127 cm^{-1} , which yields $\Delta\theta = (\text{FWHM} - 15)/6$. $tr(\epsilon)$ manifests in *c*-Si Raman spectra through shifts in the TO peak
 128 position ω [37, 38]. Strubbe et al. [39] demonstrated an empirical relationship between TO peak shifts and local
 129 strain in *a*-Si:H, which is valid for isotropic amorphous vibrational mode frequencies. In vibrational density of states
 130 calculations, the TO peak vibrations remain almost unaffected by the presence of H atoms, which indicates that
 131 atomic interactions are mostly determined by the nature of Si-Si bonds [39]. Experimental Raman spectra of *a*-Si
 132 and *a*-Si:H around the TO peak region are quite similar. Therefore, the empirical relationship obtained for *a*-Si:H is
 133 also valid for *a*-Si, and establishes $\omega = s \text{tr}(\epsilon) + \omega_0$, where $s = -460 \pm 10 \text{ cm}^{-1}$ is a fitting parameter and $\omega_0 \approx 480$
 134 cm^{-1} is the bulk *a*-Si TO peak position [36].

135 E. Double-paddle oscillator

136 Transverse sound velocity (v_t) measurements of *a*-Si films were taken at 300 mK using the double-paddle oscillator
 137 (DPO) technique described elsewhere [40, 41]. The resonant frequency of the second antisymmetric torsional resonance
 138 mode (AS2) at $\sim 5500 \text{ Hz}$ is measured to an accuracy of $<10^{-5} \text{ Hz}$ on both the bare and film-laden oscillator. The
 139 shear modulus G is measured and v_t is then calculated as $v_t = \sqrt{G/\rho}$, where ρ is the film mass density.

140 F. Electron paramagnetic resonance

141 Electron paramagnetic resonance measurements were used to determine the dangling bond density of the films, using
 142 a Bruker ELEXSYS E580 EPR spectrometer with an X-band ER 4123D CW-Resonator at 9.36 GHz. EPR determines
 143 the density of dangling bond defects, or unpaired electrons, by measuring the signal strength of the resonant transition
 144 between the Zeeman split energy levels of the paramagnetic dangling bond defect. Microwave power (1.5 mW) and
 145 magnetic field modulation amplitude (5 G) were adjusted for optimum intensity without line shape distortion. Spectra
 146 were measured from 3282 to 3383 G. A bare substrate was used to determine the background contribution, whereas
 147 the samples spin density N_S was determined by double integration of the experimental absorption first derivative
 148 spectra and by comparison to a KCl weak pitch with $N_S = 9.5 \times 10^{12} \pm 5\% \text{ spins/cm}^3$ and $g = 2.0028 \pm 0.0002$. These
 149 experimental conditions yielded N_S with a systematic error of $\sim 10\%$. The EPR spectra obtained for the *a*-Si samples
 150 studied in this work are isotropic with a Landé g -factor of 2.0055, typical of *a*-Si dangling bonds [42].

151 G. Doppler broadening spectroscopy

152 Positron annihilation experiments using DBS were performed to obtain the volume of empty space, or total volume
 153 of nanovoids, as a function of sample depth. Amorphous silicon films were grown on *c*-Si substrates with the native
 154 oxide left intact on the substrate. In order to avoid attenuation from the native oxide on the *a*-Si surface, the films were
 155 etched in a buffered oxide etch (BOE) 10:1 solution for 10 minutes, then introduced into the measurement chamber
 156 and brought below 10^{-5} Torr within 25 minutes. After BOE the S -parameter values obtained from the surface of
 157 the *a*-Si films were > 1.04 (see S definition below), typical of *a*-Si without native oxide. The vacuum pressure during
 158 typical measurements was less than 10^{-7} Torr . The positron incident beam energy was varied from 50 eV to 25 keV,
 159 which in *c*-Si yields implantation depths around 1 nm to 3 μm , respectively. In the present study, 25 keV yielded
 160 an implantation depth in the films' substrate; and data analysis is limited to below 40 keV to avoid systematic error
 161 from backscattered positrons that annihilate from the steel vacuum chamber walls.

162 A summary of DBS measurement and analysis procedures can be found elsewhere [43]. Photons emitted by positron
 163 annihilation were detected with a high purity germanium detector from EG&G Ortec, with an energy resolution of
 164 1.45 keV FWHM at the photon energy equivalent to the rest mass of positrons and electrons at 511 keV. To analyze
 165 Doppler broadening due to annihilations from nanovoids, we examined the photoelectric peak from 5×10^4 to 6×10^4
 166 detected annihilations after suitable background subtraction. The accumulated events N_c in a narrow 1.45 keV window
 167 around the center and in the two wing regions N_w are compared to the total event number in the full photoelectric
 168 peak N_{tp} . The DBS parameters S and W are the ratios of N_c/N_{tp} and N_w/N_{tp} , respectively. The beam energy E
 169 in keV is converted to implantation depth d using the empirical formula $d[nm] = 40 E^{1.6}/\rho$, where $\rho = 2.329 \text{ g/cm}^3$
 170 is the *c*-Si mass density [44]. VEPFIT software [45] is used to simulate the empty volume depth profiles optimizing
 171 S , layer thickness and positron diffusion lengths, while layer density is set to that of *c*-Si. The S -parameter yields
 172 information about the number of nanovoids and their size, from atomic vacancies to nanovoids [46]. The W -parameter
 173 is sensitive to higher momentum electrons and probes the elemental type of the nearest neighbor [47].

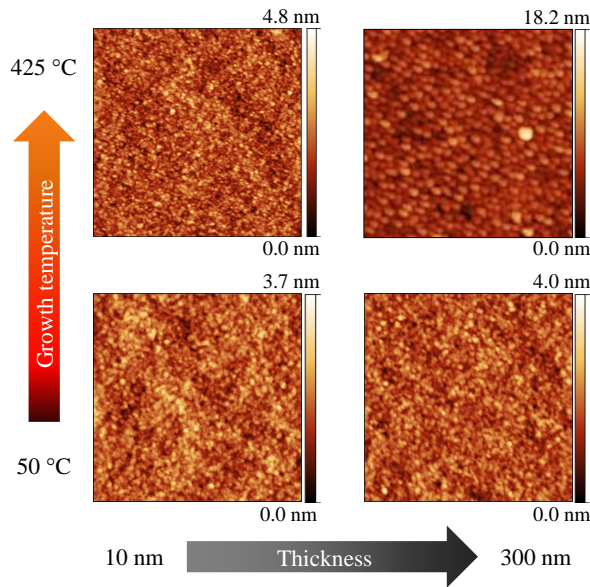


Figure 1. AFM images of the surfaces of a subset of *a*-Si films: 10 and 300 nm thick, left and right, respectively, grown at 50 °C and 425 °C, bottom and top, respectively. The scale bars at the right side of each image show the absolute height variations for each film. All images are $1 \times 1 \mu\text{m}^2$.

III. RESULTS

In this section we present the results for different properties as a function of growth temperature, growth rate and thickness. We follow the same structure presented in II, showing first the results that provide insight into the structure and network, and later the structural defects: dangling bonds and nanovoids.

Topography, roughness and stress, atomic density, bond angle deviation and local strain and nanovoids characterization were obtained from the same films; whereas other properties required films grown on specific substrates each. The errors reported in this work reflect measurement uncertainty.

A. Topography, roughness and stress

Figure 1 shows AFM images of samples grown at different temperatures and thicknesses. These images show the topography of the films' surface, where the roughness is considerably increased for thick films grown at high temperature. The statistical analysis of the images yields an average in plane grain diameter ~ 12 nm for all films, except for the thick films grown at 425 °C that show grains of ~ 20 nm. These grains measured by AFM are likely to be the end of amorphous columns observed previously in similar *a*-Si films [12].

The root mean square roughness Rq is shown in Fig. 2 as a function of thickness for films grown at 50 °C, 225 °C and 425 °C. Rq is less than 0.5 nm, the same as the roughness of the substrate, for films grown at 50 °C at all thicknesses. At higher growth temperature, Rq increases proportionally to growth temperature and with thickness up to ~ 100 nm, where it plateaus or slowly increases. A similar dependence of the surface roughness with thickness has been reported in hydrogenated *a*-Si films grown above room-temperature [48, 49].

The stress of *a*-Si films grown at room-temperature was measured through the curvature of their substrates reporting tensile stresses of 694 ± 94 MPa for a 30 nm film, and 523 ± 20 MPa for a 90 nm film, which is comparable to other *a*-Si films grown by e-beam [50].

B. Atomic density

Atomic density n_{at} of *a*-Si films grown at different temperatures and rates was determined by RBS measurements in combination with profilometry, where the thicknesses were corrected after the AFM measured roughness, as discussed in II B. The resulting data are shown in Fig. 3 as a function of thickness, which shows a remarkable and systematic

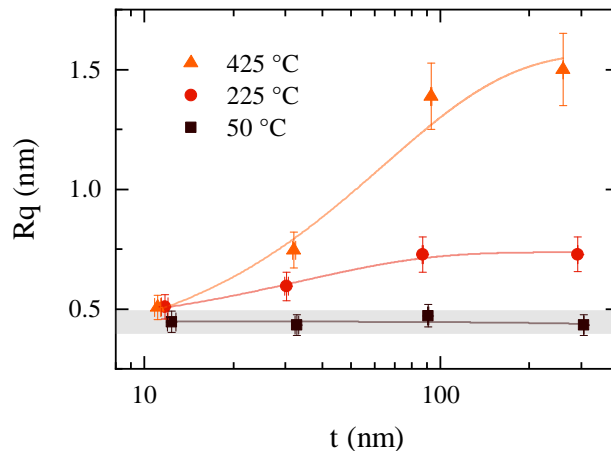


Figure 2. RMS roughness R_q of a -Si films as a function of thickness t for samples grown at 50 °C (brown squares), 225 °C (red circles) and 425 °C (orange triangles). All samples are grown at 0.5 Å/s. The gray area shows the substrate RMS roughness. Lines are guides to the eye.

199 dependence on thickness, growth temperature and rate. Error bars are dominated by the thickness uncertainty (pro-
 200 filometry) for thin films, and by areal atomic density uncertainty (RBS) for thick films. No observable discontinuities
 201 are seen. The lowest density films are quite underdense, $\sim 22\%$ less than c -Si, whereas the highest density films are
 202 $\sim 1\%$ less dense than c -Si. Previous work on vapor deposited a -Si films reported densities 19% smaller than that of
 203 c -Si [51], which was there suggested to be caused by low-density regions or nanovoids found in a -Si [52].

204 Atomic density of a -Si films grown by e-beam is thus highly dependent on thickness, growth temperature and rate.
 205 We report density reductions with thickness for a -Si samples grown at room-temperature between 25% and 10% for
 206 the thinnest and thickest films, respectively, when compared to c -Si density. Higher growth temperature and lower
 207 growth rate yield films with higher atomic density at any given thickness. Thick a -Si films, around 600 nm thick,
 208 and grown at different temperatures were subsequently annealed at 425 °C in UHV for 3 hours. The film grown at
 209 50 °C shows a thickness reduction from 598.6 nm to 593.1 nm (-5.5 ± 2.1 nm), which corresponds to a densification
 210 of $\sim 0.9\%$, whereas the thickness variation for films grown at 225 °C and 425 °C is within error bars. Annealing at
 211 temperatures up to 425 °C thus does very little to the atomic density of a -Si films.

212 Atomic density provides a proxy to evaluate the thermodynamic and kinetic stability of amorphous solids [53], where
 213 it is known that stability can be tuned by means of growth temperature and rate on vapor-deposited glasses [54].
 214 Increasing growth temperature increases surface mobility during deposition and allows atoms to reach lower energy
 215 positions before being deposited over [55]. Similarly, slower growth rates allow these positions to be reached before
 216 mobile atoms are deposited over. In the particular case of a -Si and for the data presented in this work, atomic density
 217 shows a stronger dependence on growth temperature and thickness rather than growth rate. For this reason, we focus
 218 the present study on growth temperature and thickness dependence.

219 Resonant Rutherford backscattering spectrometry was performed to determine the oxygen content through the
 220 samples. The oxygen concentration of the a -Si films ranges between 0% and 3% and shows no correlation with
 221 thickness, growth temperature or growth rate. Oxygen content did not increase with film aging (after 4 months).
 222 Neither contaminants nor water were observed via RBS and ERDA, respectively, in the films. Thickness measurements
 223 were also performed both immediately and four months after deposition, no changes were observed in thickness as a
 224 function of time.

225 C. Short- and Medium-range order

226 In this section we present electron microscopy results, specifically diffraction, EELS, FEM, and high-resolution
 227 imaging results for ~ 30 nm thick a -Si samples grown at 0.5 Å/s, and at 50 °C, 250 °C and 450 °C.

228 Figure 4 shows the average diffracted intensities $I(k)$. (k defined as $k = \theta/\lambda$, where λ is the electron wavelength.)
 229 The peak positions are typical of a -Si and do not shift significantly from sample to sample. The first broad peak sits
 230 at 3.08 ± 0.05 nm $^{-1}$, which matches the c -Si $\langle 111 \rangle$ peak at 3.13 nm $^{-1}$. The second a -Si peak position at 5.54 ± 0.05
 231 nm $^{-1}$ sits between the c -Si reflections $\langle 220 \rangle$ at 5.2 nm $^{-1}$ and $\langle 311 \rangle$ at 6.1 nm $^{-1}$. None of the data show the sharp
 232 peaks that would indicate nanocrystallization. Isolated nanocrystals were observed in the 450 °C film, indicating that
 233 under these growth conditions crystallization of a -Si starts at a temperature between 425 °C and 450 °C. Electron

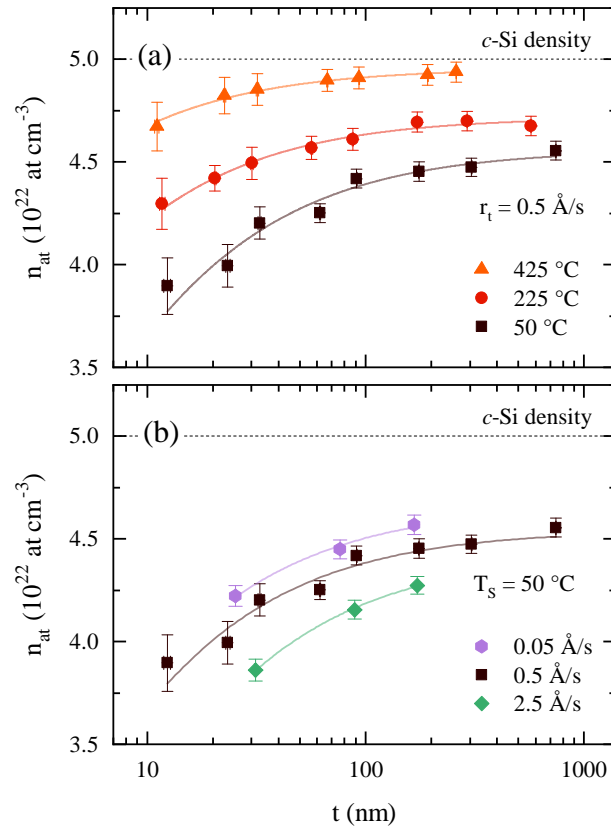


Figure 3. Atomic density n_{at} of a -Si films as a function of thickness t for (a) growth temperatures of 50 °C (brown squares), 225 °C (red circles) and 425 °C (orange triangles), and (b) growth rates of 0.05 Å/s (lilac hexagons), 0.5 Å/s (brown squares) and 2.5 Å/s (green diamonds). In (a), all films are grown at 0.5 Å/s, and in (b), all films are grown at 50 °C. In both plots the c -Si density is given for reference (dashed horizontal line). Solid lines are guides to the eye.

234 microscopy characterization was performed between the nanocrystals on fully amorphous regions. Differences in peak
 235 heights between films are not well quantified in this data. For more quantitatively accurate $I(k)$ and structure factor
 236 $S(q)$, synchrotron experiments are needed. Similarities between positions and widths for both low and high- k peaks
 237 seen in Fig. 4, however, suggest that there are no significant differences in SRO for the films grown at different
 238 temperatures, consistent with previous work on a -Si [27].

239 EELS measurements performed on the same samples find an average bulk plasmon peak energy λ_0 of 16.6 eV.
 240 The relative change in λ_0 , $\Delta\lambda/\lambda_0$ is +0.2%, +0.5%, and -0.7% for samples grown at 50 °C, 250 °C and 450 °C,
 241 respectively (Fig. 4 inset). No significant change in average bond length between the films is observed. At constant
 242 composition and temperature, $\Delta\lambda/\lambda_0 \propto \sqrt{\Delta\rho/\rho_0}$, so the maximum change in density, not counting contributions
 243 from voids, is negligible. Together, these results show that the average bond length for atoms within the network is
 244 the same for the different samples. The SRO structure, specifically bond length and coordination, is independent of
 245 the growth conditions, and there is no change in atomic number density except what is created by introducing voids,
 246 to be discussed below.

247 FEM data of the same films shown in Fig. 4 are shown in Fig. 5. $V(k)$ peaks in amorphous materials typically
 248 occur at the same k as peaks in $I(k)$. That is the case for the film grown at 50 °C, but the films grown at 250 °C and
 249 450 °C show a splitting of the first peak into a contribution near 3.1 nm^{-1} , common for all a -Si films, and another
 250 peak at lower k , closer to 2.6 nm^{-1} , which arises from some fraction of the atoms. This lower k peak indicates that
 251 local structures exist in the higher substrate temperature samples with a larger interatomic spacing than has been
 252 observed in any previous FEM experiments on a -Si. There are no larger interatomic spacings in diamond structure
 253 Si, but a different crystal structure for Si, Si24, which has diffraction features at lower k corresponding to the peak
 254 position in $V(k)$ [56]. The low- k diffraction in Si24 arises from 8-membered rings. In that work [56], the Si24 crystal
 255 was synthesized at high pressure with Na atoms embedded in the crystal, filling the 8-atom Si rings. The material was
 256 brought to room pressure, and the Na atoms were removed using thermal degassing. The resulting crystal is stable at
 257 room-temperature and atmospheric pressure. We do not suggest that there are nanocrystals of Si24 in the material, or

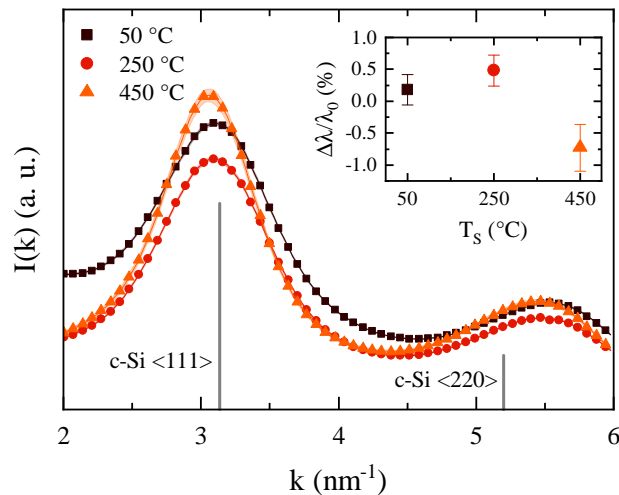


Figure 4. Diffracted electron intensity $I(k)$ for a -Si thin films, ~ 30 nm thick, grown at $0.5 \text{ \AA}/\text{s}$, and at $50 \text{ }^\circ\text{C}$ (brown), $250 \text{ }^\circ\text{C}$ (red) and $450 \text{ }^\circ\text{C}$ (orange). The diffraction peaks of c-Si are shown for reference. Shaded areas behind the data show their associated error. Inset: Bulk plasmon relative change $\Delta\lambda/\lambda_0$ from EELS as a function of growth temperature T_s for the same samples.

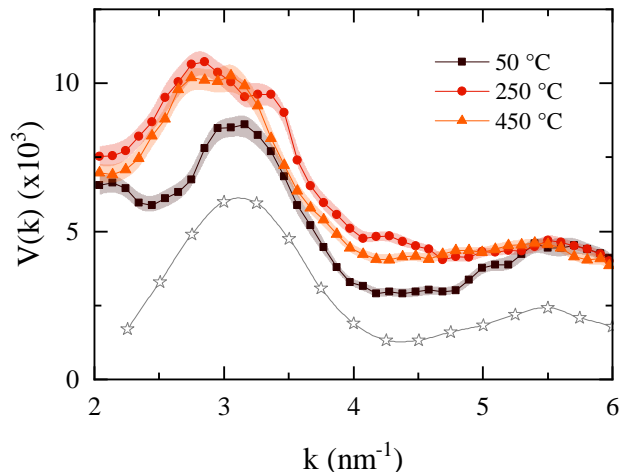


Figure 5. FEM data $V(k)$ as a function of wavevector k of a -Si thin films, ~ 30 nm thick, grown at $0.5 \text{ \AA}/\text{s}$, and at $50 \text{ }^\circ\text{C}$ (brown squares), $250 \text{ }^\circ\text{C}$ (red circles) and $450 \text{ }^\circ\text{C}$ (orange triangles). Shaded areas behind the data show their associated error. Grey stars show MRO typically observed in a -Si films from Ref. [30]. The data for the $250 \text{ }^\circ\text{C}$ and $450 \text{ }^\circ\text{C}$ films, however, reveal a MRO structure not previously reported.

258 even that we have created a paracrystalline analog to Si24. Instead we suggest that the low- k feature in $V(k)$ of these
 259 a -Si films grown at higher temperatures ($225 \text{ }^\circ\text{C}$ and $425 \text{ }^\circ\text{C}$) could be caused by structures in the amorphous network
 260 involving large rings of 8 atoms or more, significantly larger than those typically present in a -Si [57]. These could
 261 even be viewed as extremely tiny nanovoids. However, we do not have a detailed structural model that quantitatively
 262 reproduces the FEM data, and alternatively the FEM data of the a -Si films grown at higher temperatures can also
 263 be explained as the diffraction signal from atoms on the surface of nanovoids.

264 Fig. 6 shows under-focus, in-focus, and over-focus HRTEM images of the same samples. Under- and over-focus
 265 image pairs are a classical method for identifying voids in materials from the switch in contrast of the Fresnel fringe
 266 surrounding the void. The $50 \text{ }^\circ\text{C}$ sample shows clear evidence of columnar microstructure with nanometer-scale voids
 267 forming part of the column boundaries. The higher temperature films do not have the columnar microstructure and
 268 do not have voids detectable by this method. In our previous work [12], cross-sectional TEM images (XTEM) of
 269 a -Si films shown a columnar structure whose diameter increases with growth temperature. Such structure is common
 270 in amorphous films grown by PVD techniques [58], including e-beam evaporation [59]. These images also reveal a
 271 region close to the substrate interface that lacks columnar microstructure; this region is thicker for higher growth

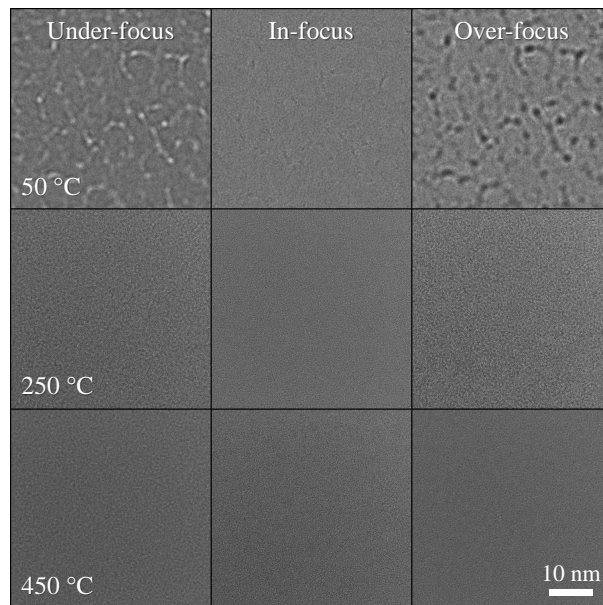


Figure 6. HRTEM images of *a*-Si thin films ~ 30 nm thick grown at 0.5 \AA/s and at $50 \text{ }^\circ\text{C}$, $250 \text{ }^\circ\text{C}$ and $450 \text{ }^\circ\text{C}$ (top to bottom row, respectively). Columns from left to right show under-focus, in-focus, and over-focus images (see description in text). The film grown at $50 \text{ }^\circ\text{C}$ shows columnar structure, visible as wiggly lines and voids visible as white features in the under-focus image and black features in the same place in the over-focus image. Films grown at higher temperatures show no notable features.

temperature. The columnar structure observed for the film grown at $50 \text{ }^\circ\text{C}$ has not developed yet for films grown at $250 \text{ }^\circ\text{C}$ and $450 \text{ }^\circ\text{C}$; therefore, the thickness at which columns develop in *a*-Si thin films is growth temperature dependent.

D. Bond angle deviation and local strain

Electron microscopy was used as described above to characterize SRO. $I(k)$ and $\Delta\lambda/\lambda_0$ are mostly sensitive to bond length and coordination number, and less to bond angles. We here turn to Raman to characterize the deviations from the tetrahedral angle θ that are found in *a*-Si. Figure 7(a) shows the bond angle deviation $\Delta\theta$ as a function of thickness for a series of growth temperatures. The range of $\Delta\theta$ found for these samples, approximately 9° to 13° , is similar to values reported for *a*-Si model structures [34]. Films grown at $425 \text{ }^\circ\text{C}$ show $\Delta\theta$ that ranges from 9° to 10° . These values fall on the low end of those obtained from the radial distribution function of *a*-Si [6]; and to our knowledge are amongst the lowest reported by experiment. Note that $\Delta\theta = 0^\circ$ for c-Si, and has been shown theoretically to be $\geq 6.6^\circ$ for *a*-Si [34], evidence that the transition from crystalline to amorphous structures is not continuous. $\Delta\theta$ is considered a measure of disorder at very short length scales; nearest neighbor distances, or around 2 \AA . At each thickness, $\Delta\theta$ is lower for films grown at higher temperatures, indicating that disorder decreases with increasing growth temperature.

Figure 7(b) shows the trace of the local strain $tr(\epsilon)$ calculated from ω as described in IID. $\Delta\theta$ and $tr(\epsilon)$ shown in Figs. 7(a) and 7(b), respectively, are correlated. Higher growth temperature thus yields less disordered and less strained films at all thicknesses. However, the monotonic trend observed for atomic density as a function of thickness is not seen for these properties: both $\Delta\theta$ and $tr(\epsilon)$ increase with thickness up to a maximum value, then decrease. This behavior is most clear in films grown at $50 \text{ }^\circ\text{C}$, where the maximum values of $\Delta\theta$ and $tr(\epsilon)$ occur near 30 nm . For films grown at higher temperature, the peak in $\Delta\theta$ and $tr(\epsilon)$ is more subtle, and may occur at a different thicknesses.

Raman data analysis shows a relaxation process in which disorder and local strain reduce above a *critical thickness*; however, it is unclear whether this process implies a structural change in the atoms underneath, i.e., the *reorganization* of the atoms already deposited.

Following the procedure described in II, we study n_{at} and $\Delta\theta$ of several *a*-Si etched films. In Fig. 8 we compare these results to equivalent as-deposited films to probe for reorganization during growth. The larger error bars are due to increased surface roughness and thickness uncertainty after the etch process. All films etched and measured were grown at $50 \text{ }^\circ\text{C}$ because they exhibit the largest change in atomic density and bond angle deviation as a function

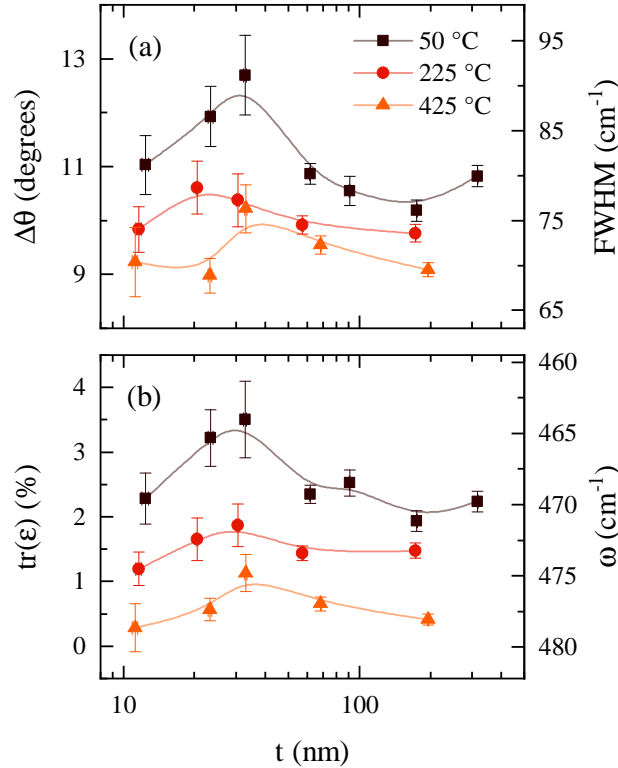


Figure 7. (a) Bond angle deviation $\Delta\theta$ and (b) trace of strain $tr(\epsilon)$ as a function of thickness t for samples grown at 50 °C (brown squares), 225 °C (red circles) and 425 °C (orange triangles). Right axis in both panels show the measured quantity from which $\Delta\theta$ and $tr(\epsilon)$ are calculated as described in the text. Lines are guides to the eye.

of thickness, as seen in Figs. 3(a) and 7(a), respectively. The gray areas labeled ‘reorganization’ in Fig. 8 are the extrapolated n_{at} and $\Delta\theta$ values of thick as-deposited films. A complete reorganization would yield etched thin films with the higher n_{at} and lower $\Delta\theta$ of the as-deposited thicker films, whereas a lack of reorganization would yield etched thin films with the lower density and higher disorder of the as-deposited thin films.

Fig. 8(a) shows that atomic density n_{at} from etched films is higher than that of as-deposited films with similar thickness, most consistent with reorganization, with etched films lying within error bars of the as deposited values of thick films and well above the values of as-deposited thin films. Bond angle deviation $\Delta\theta$ from etched films is lower than that of as-deposited films with similar thickness, shown in Fig. 8(b), which suggests a reduction of disorder, and are also most consistent with reorganization of the early layers of atoms deposited near the substrate.

It has been proposed that due to the large interface energy between substrate and film, thin films prepared by physical vapor deposition grow via a Volmer-Weber mode [60, 61]. This proposed growth mode is in agreement with stress measurements in e-beam evaporated a -Si films, which show the nucleation of columns that correlate with the transition from compressive to tensile stress regimes as a function of thickness [50].

The results presented in this section show structural relaxation as a function of thickness that leads to the reduction of disorder and local strain, compatible with the previously described studies of the stress evolution during growth of evaporated a -Si [50]. From this work [50], we also see that the dependence with thickness of the compressive-to-tensile stress transition is in agreement with our structural observations by XTEM, which show the onset of the columnar growth [12].

E. Transverse sound velocity

Transverse sound velocity v_t as a function of thickness for films grown at different temperatures is shown in Fig. 9. Sound velocity is only weakly dependent on thickness, perhaps within error bars of constant, whereas it increases with increasing growth temperature.

Sound velocity in solids, including amorphous solids, is due to phonons that propagate through the material, with a velocity that is independent of the frequency of the phonons for relatively long wavelength phonons. The sound

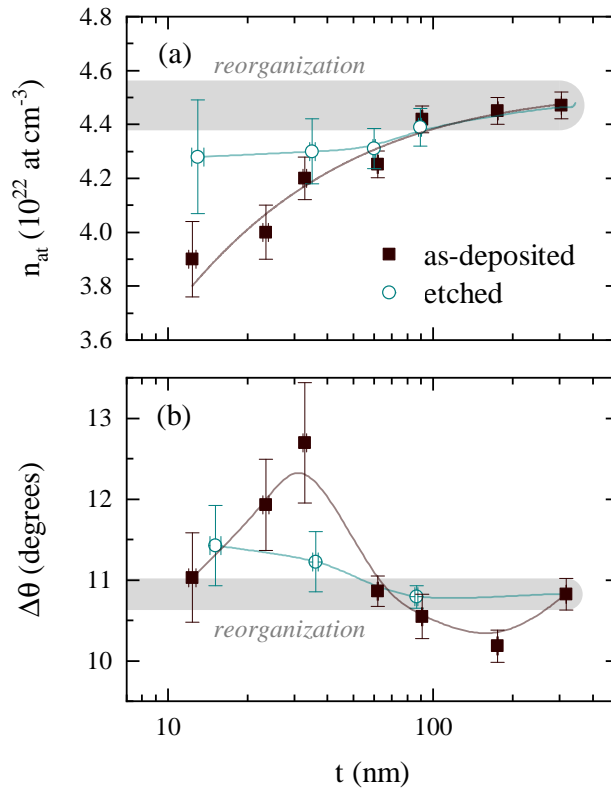


Figure 8. (a) Atomic density n_{at} , and (b) bond angle deviation $\Delta\theta$ as a function of thickness t for as-deposited (brown closed squares) and etched (cyan open circles) films. All films were grown at 50°C and $0.5 \text{ \AA}/\text{s}$; etched films initially were ~ 300 nm thick. Gray areas labeled ‘reorganization’ show the extrapolated n_{at} and $\Delta\theta$ values of the ~ 300 nm as-deposited films prior to the etch process (see text for further details). Lines are guides to the eye.

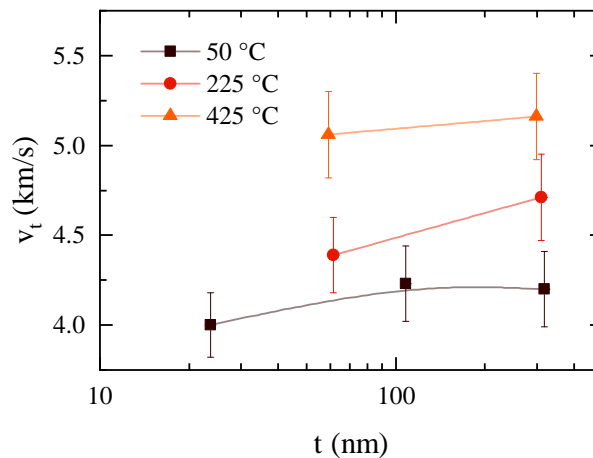


Figure 9. Transverse sound velocity v_t as a function of thickness t of a -Si films grown at 50°C (brown squares), 225°C (red circles) and 425°C (orange triangles). Lines are guides to the eye.

324 velocity is generally dependent on the interatomic spacing, the atomic mass, and the interatomic bond strength.
 325 In a -Si, the increase of sound velocity v_t with increasing growth temperature, shown in Fig. 9, correlates with the
 326 reduction of atomic disorder ($\Delta\theta$) and local strain ($tr(\epsilon)$), shown in Figs. 7(a) and 7(b), respectively. That sound
 327 velocity depends strongly on growth temperature, but is not strongly dependent on thickness at constant growth
 328 temperature, despite significant changes in atomic density with thickness, shows that sound waves are carried through
 329 an a -Si network. Sound velocity, therefore, is not affected directly by the overall density, i.e., it is not much affected
 330 by nanovoids.

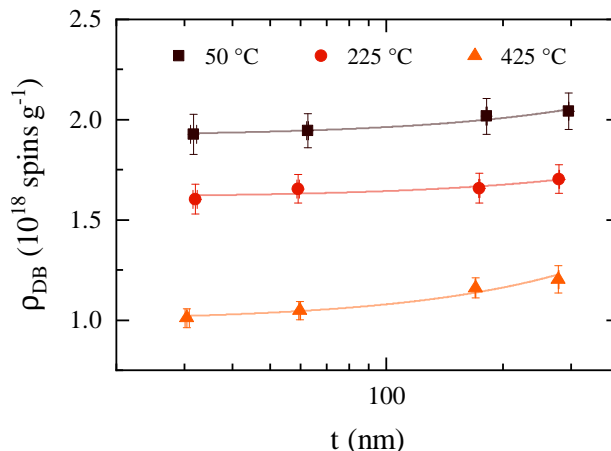


Figure 10. Dangling bond density ρ_{DB} as a function of thickness t of a -Si films grown at 50 °C (brown squares), 225 °C (red circles) and 425 °C (orange triangles). All samples were grown at 0.5 Å/s. Lines are linear fits to the data.

331

F. Dangling bond density

332 Dangling bond density ρ_{DB} has long been considered a defect metric and is correlated with surface-state transitions
 333 in silicon [62]. In photovoltaic and semiconductor technologies, a -Si is prepared with hydrogen in order to passivate
 334 dangling bonds and create high quality, or device quality, films. The dangling bond densities of our films are on the
 335 order of 10^{18} spins/cm³ (see Fig. 10). Standard a -Si has dangling bond densities $\sim 10^{19}$ spins/cm³, and device-quality
 336 a -Si:H shows values $< 10^{16}$ spins/cm³ [63]. We report ρ_{DB} per unit mass (g^{-1}) rather than per unit volume (cm^{-3})
 337 because the atomic density of our samples is not constant, which makes the former a more accurate metric for direct
 338 comparisons.

339 Figure 10 shows that ρ_{DB} decreases significantly with increasing growth temperature, and mildly increases with
 340 thickness for all growth temperatures. The former statement is consistent with the strong dependence of atomic density
 341 n_{at} on growth temperature, but is the opposite to how n_{at} depends on thickness, suggesting that the relationship
 342 between n_{at} and ρ_{DB} is not simple. The dependence of ρ_{DB} on growth temperature suggests that the nucleation of
 343 dangling bonds is inversely proportional to surface diffusion; specifically, that higher growth temperature yields more
 344 4-fold coordinated atoms. That dangling bond density mildly *increases* with thickness for all growth temperatures,
 345 suggests that the formation of this type of defect is not related to the mechanisms responsible for the films' atomic
 346 density or the atomic reorganization process previously discussed.

347 The short- and medium-range order, bond angle deviation, local strain and dangling bond density results report
 348 information about the distribution of silicon atoms in the films and about specific electronic defects; specifically, EELS
 349 results show that the interatomic distances do not change with growth temperature. Therefore, these results do not
 350 explain the very low atomic density values, and particularly that of the thinnest films grown at room-temperature.
 351 In the next section, we study the presence of nanovoids, which in a -Si cannot be detected by microscopy techniques,
 352 but are considered a common structural defect in a -Si [64].

353

G. Nanovoids characterization

354 Doppler broadening spectroscopy results for films of different thicknesses and grown at 50 °C are shown in Fig. 11,
 355 where the S -parameter is plotted as a function of energy. Energy is proportional to penetration depth (as described
 356 in II G) and, for the films reported in this work, it ranges from 0 keV (surface) to ~ 30 keV (substrate) for the thickest
 357 films. We could not measure films thinner than 60 nm due to lack of sensitivity. In this work, the data acquired from
 358 the annihilation of positrons indicate that all a -Si films measured, grown at different temperatures and for different
 359 thicknesses, contain nanovoids. Specifically, the normalized S -parameter S/S_{c-Si} values are associated to nanovoids
 360 with at least five missing atoms ($n = 5$) [46]. The correspondence between S/S_{c-Si} and n is established for nanovoids
 361 with $n < 6$ [65], whereas the size of larger nanovoids is extrapolated from the previous correspondence and should be
 362 taken with caution [46]. Electron microscopy cannot detect the presence of nanovoids in a -Si films due to the atomic
 363 superposition and the low atomic scattering factor of silicon. For these reasons, we can only provide a lower bound
 364 for nanovoids with more than six missing atoms.

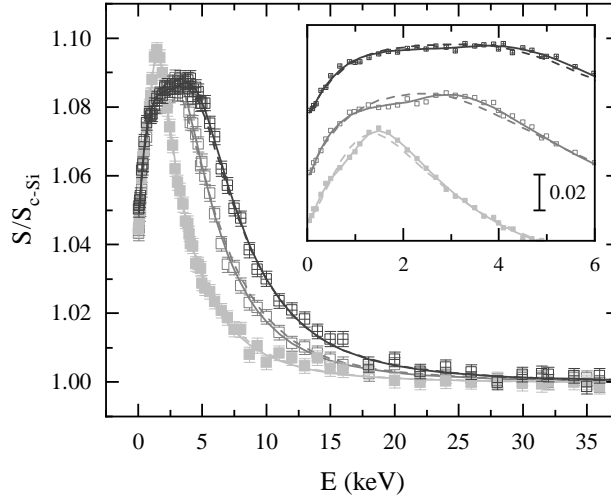


Figure 11. S -parameter normalized to the c-Si S -parameter ($S_{c-Si} = 0.5324$) as a function of incident positron energy E of three a -Si films grown at $50\text{ }^\circ\text{C}$ and 0.5 \AA/s , with thicknesses of 66 nm, 183 nm and 308 nm (light to dark grey, respectively). Data at 0 keV are values from the a -Si surface, and move progressively through the film for increasing energies until the beam reaches the substrate at ~ 30 keV. Inset: detail at low energies showing the accuracy of the single (dashed lines) and dual (solid lines) models. The dual model improves its relative accuracy with respect to the experimental data almost 50% compared to the single model. Curves have been vertically shifted to better show the fittings.

365 We used two different models to simulate the experimental data [66]: 1) a *single* volume of empty space that
 366 is uniformly distributed throughout the film, and 2) a *dual* volume of empty space that are uniformly distributed
 367 throughout the film, in which the nanovoids volume closer to the substrate is different than that closer to the surface.
 368 The simulations yield better results for the dual model, which is almost 50% more accurate than the single model (see
 369 inset in Fig. 11). The dual volume of empty space is the simplest model to probe whether the data suggests a more
 370 complex distribution of nanovoids than a single volume of empty space model. These results suggest that, at least,
 371 two different distributions of nanovoids are present on a -Si films thicker than 60 nm, with the interface between the
 372 two distributions at 31 ± 6 nm from the substrate for films grown at $50\text{ }^\circ\text{C}$, and at 59 ± 17 nm for films grown at 425
 373 $^\circ\text{C}$. This increase of the first nanovoids layer thickness with growth temperature is in agreement with the thickness
 374 dependence of void tracks formation with growth temperature seen in a -Si films grown by Floro et al. [50]. The dual
 375 model also reports that the first layer, closer to the substrate, has a larger volume of empty space than the second
 376 layer, closer to the surface. Specifically, for the first and second layers we obtain > 25 and 6 missing atoms for films
 377 grown at $50\text{ }^\circ\text{C}$, and > 19 and 5 missing atoms for films grown at $425\text{ }^\circ\text{C}$, respectively.

378 S vs W plots are shown in Fig. 12 for the same films shown in Fig. 11 and a ~ 300 nm film grown at $425\text{ }^\circ\text{C}$.
 379 Typical S vs W plots show annihilated positrons with a constant S/W ratio from surface to substrate (a single
 380 straight line). Our results, however, show a “V” shaped line due to the presence of different types of nanovoids
 381 across the film (nanovoids of different size). In other words, different S - W pairs, or slopes, represent nanovoids with
 382 a chemically distinct surface bonding. Steeper S - W slopes correspond to larger nanovoids. Points at the end of
 383 the “V” with moderate S and high W values exist at the surface of the film, and progressively change by following
 384 the “V” shape to its vertex with low S and high W , where positrons annihilate at the interface between the two
 385 distinct distributions of nanovoids (see Fig. 12 and corresponding labels). The chemical change of the nanovoids across the
 386 distinct distributions is due to the distinct chemical nature of electrons present in them, i.e., to the nanovoids sizes
 387 and not to their concentration.

388 The analysis of the S data suggests that a single distribution is less likely than a dual distribution of empty space
 389 volume, or total nanovoids volume, as shown in Fig. 11 inset, and the S - W data in Fig. 12 shows more than one
 390 type of nanovoid, which significantly differ in the nature of the bonding at their inner surfaces. Films grown at all
 391 temperatures show that the distribution closer to the surface has a smaller empty space volume than the distribution
 392 closer to the substrate. Additionally, the empty space volume in the distribution closer to the surface is smaller for
 393 films grown at $425\text{ }^\circ\text{C}$ compared to films grown at $50\text{ }^\circ\text{C}$.

394 In a -Si, dangling bonds are found to occur on the inner surfaces of nanovoids [67–70]. However, the relationship in
 395 the literature between dangling bonds and nanovoids is unclear.

396 The existence of nanovoids in a -Si, confirmed by DBS measurements, provides an explanation for the the low atomic
 397 density values of the films reported in this work.

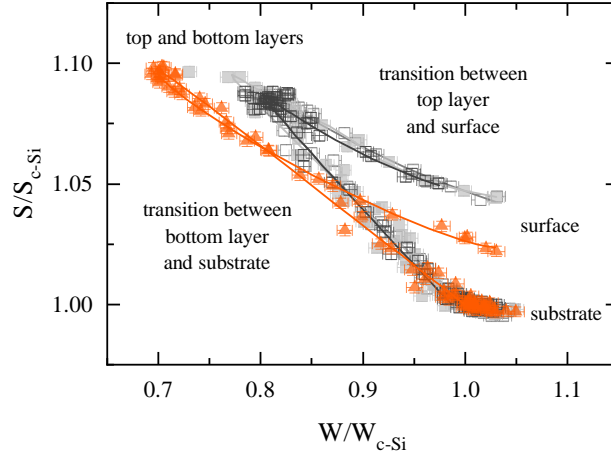


Figure 12. S vs W plots for films grown at 50 °C, with 66 nm, 183 nm and 308 nm (light to dark grey squares, respectively), and for a film grown at 425 °C with 291 nm (orange triangles). Vertical and horizontal axes are normalized to the c-Si S and W values, with $S_{c-Si} = 0.5324$ and $W_{c-Si} = 0.0237$. Solid lines are S - W fits considering a bilayer distribution of nanovoids. Labels indicate the position where positrons annihilate from film surface to substrate.

398

IV. DISCUSSION AND CONCLUSIONS

399 Atomic density n_{at} of a -Si films increases with increasing growth temperature and thickness, and with reducing
 400 growth rate (Fig. 3). In all cases films are underdense, with n_{at} as high as $\sim 99\%$ of c-Si density for films grown at
 401 425 °C and thicker than 300 nm, and as low as $\sim 78\%$ of c-Si density, which is achieved for the thinner films grown
 402 at room-temperature. FEM results on ~ 30 nm thick films show significant differences in MRO, as shown in Fig. 5,
 403 despite no change in SRO (Fig. 4), which suggests that larger membered rings appear as the growth temperature
 404 increases. Measurements of the plasmon peak energy relative change $\Delta\lambda/\lambda_0$ presented in the inset of Fig. 4, show no
 405 significant changes in atomic density between films as a function of growth temperature. Therefore, the reduction of
 406 n_{at} can only be attributed to voids. Those voids must be nanometer-scale, as large voids would be visible in HRTEM.

407 Raman data analysis reveals a reduction of the atomic disorder, the bond angle deviation $\Delta\theta$, with increasing
 408 growth temperature [Fig. 7(a)]. This dependence on growth temperature is also observed for the local strain $tr(\epsilon)$
 409 of the a -Si films [Fig. 7(b)]. These data show a non-monotonic behavior of disorder and local strain with thickness,
 410 particularly for films grown at room-temperature, whose magnitudes build up and then reduce to their initial values.
 411 The characterization of nanovoids shows that the best simulations of the data (Fig. 11) and the analysis of the S - W
 412 plots (Fig. 12) suggest the presence of at least two different types, or sizes, of nanovoids, with larger empty space
 413 volume near the substrate. The thickness at which the transition between the two distributions occurs, increasing
 414 from approximately 30 nm to 60 nm with increasing growth temperature, coincides with the critical thickness seen
 415 by Raman. The stress results also report higher tensile stress for thinner films, ~ 30 nm thick, than for thicker films,
 416 ~ 90 nm thick. We therefore speculate that at the critical thickness a structural relaxation process occurs, triggering
 417 the formation of columns observed by electron microscopy [12, 50], and the reduction of $\Delta\theta$ (atomic disorder) and
 418 $tr(\epsilon)$ (local strain). Floro et al. [50], see similar effects, albeit at slightly different thicknesses.

419 The study of n_{at} and $\Delta\theta$ from etched samples, Figs. 8(a) and 8(b), respectively, shows reorganization of the
 420 films' structure during growth. These results do not suggest a direct relationship between reorganization and critical
 421 thickness, even though they might be caused by a common underlying relaxation process that takes place during
 422 growth. We note that the atomic density increases monotonically with thickness, suggesting that the reorganization
 423 of the films continuously happens during growth, whereas the critical thickness seems to be triggered by an specific
 424 event. Additionally, DBS results based on a dual distribution of empty space volume show that the total volume of
 425 nanovoids reduces as films grow thicker. Our data do not allow us to establish whether reorganization and critical
 426 thickness are two processes independent of each other, or whether one is triggered by the other.

427 Dangling bond density ρ_{DB} results report up to ~ 1 defect in 10^4 atoms, which implies that Si atoms in a -Si films
 428 are largely fully coordinated despite their notably low atomic densities in some films, with up to $\sim 22\%$ missing atoms
 429 (compared to c-Si). These results suggest that only a very small fraction (less than 1%) of nanovoids contain even one
 430 dangling bond. Additionally, energetic considerations suggest that having two dangling bonds in a single nanovoid is
 431 unlikely because two nearby under-coordinated silicon atoms will bond together. Therefore, the increase of ρ_{DB} with
 432 thickness (Fig. 10) suggests an increase of the nanovoid number, which in combination with the densification of the

433 films (Fig. 3) imply that nanovoids become smaller as films grow thicker. This conclusion is also supported by DBS
 434 results (Fig. 12).

435 Two distinct processes happen in e-beam evaporated *a*-Si films during growth: i) a sudden structural relaxation
 436 at a *critical thickness*, which depends on growth temperature and correlates with the formation of columns [12, 50]
 437 (Figure 6). This process is also captured by the reduction of atomic disorder and local strain (Figure 7), and by the
 438 reduction of nanovoids size and their total volume (Figure 12). And ii) a continuous *reorganization* of the atoms seen
 439 in the atomic density and bond angle deviation of etched thicker films (Figure 8). This process is responsible for the
 440 reduction of the total volume of nanovoids as films grow thicker, which leads to the continuous densification of the
 441 films (Figure 3) and to the reduction of TLSs [10, 71].

442 As we previously reported, the TLS density of *a*-Si obtained from films equivalent to those presented in this work,
 443 depends strongly on growth conditions, with a dependence that can be completely explained by plotting TLS density as
 444 a function of atomic density. Remarkably, and as previously observed [10], the excess heat capacity at low temperature,
 445 below 10 K, of thinner *a*-Si films (112 nm) is larger than that of thicker films (278 nm). This observation cannot
 446 solely be explained by the larger concentration of nanovoids in the first layer (near the substrate), which indeed would
 447 yield thinner films with larger excess specific heat, but not heat capacity. This excess heat capacity reduction can
 448 only be explained by atomic reorganization, which effectively reduces the number of TLSs when films grow thicker.
 449 Similarly, the mechanical loss of thinner *a*-Si films (59 nm) is larger than that of thicker films (299 nm) [71]. Our data
 450 suggest that the structural origin of TLSs in *a*-Si likely occur in highly disordered regions where nanovoids are present.
 451 The reduction of atomic disorder and nanovoids volume (increase in atomic density) correlates with the reduction
 452 of TLSs observed in thicker *a*-Si films. The reorganization of the atoms as films grow thicker plays a crucial role in
 453 reducing TLSs in *a*-Si, and it is likely to be related to local structural rearrangements caused by structural relaxation
 454 processes. The reduction of TLSs with growth temperature is likely to be related to surface diffusion mechanisms
 455 during growth, since surface diffusion is enhanced by temperature. Additionally, Fig. 9 shows that sound velocity
 456 increases with increasing growth temperature, while its dependence on thickness is within error bars of no dependence,
 457 suggesting that the sound velocity depends on properties of the *a*-Si network, such as bond angle disorder, and not on
 458 the presence of nanovoids; while nanovoids and their environment, and not the constrained network, are responsible
 459 for the mechanisms that enable TLSs in *a*-Si.

460 ACKNOWLEDGEMENTS

461 We thank P. Ci and J. Wu for assistance with Raman measurements; R. Chatterjee and J. Cooper for assistance
 462 with EPR measurements; D. Castells-Graells for assistance with films growths; and D. Strubbe for fruitful discussions
 463 on *a*-Si:H Raman spectra calculations. Samples preparation, ion beam analysis and Raman characterization were
 464 done at UCB supported by NSF (DMR-1508828 and DMR-1809498). Electron microscopy characterization was done
 465 at UW-Madison supported by the Wisconsin MRSEC (DMR-1720415). Sound velocity characterization was done at
 466 NRL supported by the Office of Naval Research. Electron paramagnetic resonance measurements were done at LBNL
 467 Joint Center for Artificial Photosynthesis supported by DOE (DE-SC0004993). Doppler broadening spectroscopy
 468 characterization was done at WSU supported by the late Dr. Kelvin Lynn and the Center of Materials Research (now
 469 Institute of Materials Research).

-
- 470 [1] R. A. Street, ed., *Technology and Applications of Amorphous Silicon*, 1st ed., Springer Series in Materials Science, Vol. 37
 471 (Springer, Berlin, Heidelberg, 2000).
 472 [2] N.-M. Park, C.-J. Choi, T.-Y. Seong, and S.-J. Park, *Phys. Rev. Lett.* **86**, 1355 (2001).
 473 [3] W. D. Oliver and P. B. Weland, *MRS Bull.* **38**, 816 (2013).
 474 [4] R. X. Adhikari, K. Arai, A. F. Brooks, C. Wipf, O. Aguiar, P. Altin, B. Barr, L. Barsotti, R. Bassiri, A. Bell, G. Billingsley,
 475 R. Birney, D. Blair, E. Bonilla, J. Briggs, D. D. Brown, R. Byer, H. Cao, M. Constancio, S. Cooper, T. Corbitt, D. Coyne,
 476 A. Cumming, E. Daw, R. DeRosa, G. Eddolls, J. Eichholz, M. Evans, M. Fejer, E. C. Ferreira, A. Freise, V. V. Frolov,
 477 S. Gras, A. Green, H. Grote, E. Gustafson, E. D. Hall, G. Hammond, J. Harms, G. Harry, K. Haughian, D. Heinert,
 478 M. Heintze, F. Hellman, J. Hennig, M. Hennig, S. Hild, J. Hough, W. Johnson, B. Kamai, D. Kapasi, K. Komori,
 479 D. Koptsov, M. Korobko, W. Z. Korth, K. Kuns, B. Lantz, S. Leavey, F. Magana-Sandoval, G. Mansell, A. Markosyan,
 480 A. Markowitz, I. Martin, R. Martin, D. Martynov, D. E. McClelland, G. McGhee, T. McRae, J. Mills, V. Mitrofanov,
 481 M. Molina-Ruiz, C. Mow-Lowry, J. Munch, P. Murray, S. Ng, M. A. Okada, D. J. Ottaway, L. Prokhorov, V. Quetschke,
 482 S. Reid, D. Reitze, J. Richardson, R. Robie, I. Romero-Shaw, R. Route, S. Rowan, R. Schnabel, M. Schneewind, F. Seifert,
 483 D. Shaddock, B. Shapiro, D. Shoemaker, A. S. Silva, B. Slagmolen, J. Smith, N. Smith, J. Steinlechner, K. Strain, D. Taira,

- 484 S. Tait, D. Tanner, Z. Tornasi, C. Torrie, M. Van Veggel, J. Vanheijningen, P. Veitch, A. Wade, G. Wallace, R. Ward,
485 R. Weiss, P. Wessels, B. Willke, H. Yamamoto, M. J. Yap, and C. Zhao, *Class. Quantum Gravity* **37**, 165003 (2020).
- 486 [5] J. Steinlechner and I. W. Martin, *Phys. Rev. D* **103**, 042001 (2021).
- 487 [6] J. Fortner and J. S. Lannin, *Phys. Rev. B* **39**, 5527 (1989).
- 488 [7] K. Laaziri, S. Kycia, S. Roorda, M. Chicoine, J. L. Robertson, J. Wang, and S. C. Moss, *Phys. Rev. Lett.* **82**, 3460 (1999).
- 489 [8] W. A. Phillips, *J. Low Temp. Phys.* **7**, 351 (1972).
- 490 [9] B. L. Zink, R. Pietri, and F. Hellman, *Phys. Rev. Lett.* **96**, 055902 (2006).
- 491 [10] D. R. Queen, X. Liu, J. Karel, T. H. Metcalf, and F. Hellman, *Phys. Rev. Lett.* **110**, 135901 (2013).
- 492 [11] X. Liu, D. R. Queen, T. H. Metcalf, J. E. Karel, and F. Hellman, *Phys. Rev. Lett.* **113**, 025503 (2014).
- 493 [12] D. R. Queen, X. Liu, J. Karel, H. C. Jacks, T. H. Metcalf, and F. Hellman, *J. Non-Cryst. Solids* **426**, 19 (2015).
- 494 [13] W. A. Phillips, *Rep. Prog. Phys.* **50**, 1657 (1987).
- 495 [14] J. M. Martinis, K. B. Cooper, R. McDermott, M. Steffen, M. Ansmann, K. D. Osborn, K. Cicak, S. Oh, D. P. Pappas,
496 R. W. Simmonds, and C. C. Yu, *Phys. Rev. Lett.* **95**, 210503 (2005).
- 497 [15] J. Gao, J. Zmuidzinas, B. a. Mazin, H. G. Leduc, and P. K. Day, *Appl. Phys. Lett.* **90**, 2013 (2007).
- 498 [16] R. W. Simmonds, M. S. Allman, F. Altomare, K. Cicak, K. D. Osborn, J. A. Park, M. Sillanpää, A. Sirois, J. A. Strong,
499 and J. D. Whittaker, *Quantum Inf. Process.* **8**, 117 (2009).
- 500 [17] J. Steinlechner, I. W. Martin, A. S. Bell, J. Hough, M. Fletcher, P. G. Murray, R. Robie, S. Rowan, and R. Schnabel,
501 *Phys. Rev. Lett.* **120**, 263602 (2018).
- 502 [18] R. Birney, J. Steinlechner, Z. Tornasi, S. MacFoy, D. Vine, A. S. Bell, D. Gibson, J. Hough, S. Rowan, P. Sortais,
503 S. Sproules, S. Tait, I. W. Martin, and S. Reid, *Phys. Rev. Lett.* **121**, 191101 (2018).
- 504 [19] J. L. Pitters, L. Livadaru, M. B. Haider, and R. A. Wolkow, *J. Chem. Phys.* **134**, 064712 (2011).
- 505 [20] M. Morita, T. Ohmi, E. Hasegawa, M. Kawakami, and M. Ohwada, *J. Appl. Phys.* **68**, 1272 (1990).
- 506 [21] D. Misra, W. Zhong, R. A. Bartynski, V. Patel, and B. Singh, *Semicond. Sci. Technol.* **11**, 816 (1996).
- 507 [22] M. J. Madou, *Fundamentals of Microfabrication: The Science of Miniaturization*, 2nd ed. (CRC Press, 2002) Chap. 4, pp.
508 214–215.
- 509 [23] G. G. Stoney, *Proc. R. Soc. Lond. A* **82**, 172 (1909).
- 510 [24] C. A. Klein, *J. Appl. Phys.* **88**, 5487 (2000).
- 511 [25] M. Mayer, in *AIP Conf. Proc.* (AIP, 1999) pp. 541–544.
- 512 [26] P. M. Voyles, J. M. Gibson, and M. M. J. Treacy, *J. Electron Microsc.* **49**, 259 (2000).
- 513 [27] P. Voyles and D. Muller, *Ultramicroscopy* **93**, 147 (2002).
- 514 [28] J. Hwang, Z. H. Melgarejo, Y. E. Kalay, I. Kalay, M. J. Kramer, D. S. Stone, and P. M. Voyles, *Phys. Rev. Lett.* **108**,
515 195505 (2012).
- 516 [29] Y. Zhang, E. C. Glor, M. Li, T. Liu, K. Wahid, W. Zhang, R. A. Riggelman, and Z. Fakhraai, *J. Chem. Phys.* **145**, 114502
517 (2016).
- 518 [30] P. M. Voyles and J. R. Abelson, *Sol. Energy Mater. Sol. Cells* **78**, 85 (2003).
- 519 [31] N. Zotov, M. Marinov, N. Mousseau, and G. Barkema, *J. Phys.: Condens. Matter* **11**, 9647 (1999).
- 520 [32] M. Mecklenburg, W. A. Hubbard, E. R. White, R. Dhall, S. B. Cronin, S. Aloni, and B. C. Regan, *Science* **347**, 629 (2015).
- 521 [33] P. Palanisamy and J. M. Howe, *J. Appl. Phys.* **110**, 024908 (2011).
- 522 [34] D. Beeman, R. Tsu, and M. F. Thorpe, *Phys. Rev. B* **32**, 874 (1985).
- 523 [35] M. Marinov and N. Zotov, *Phys. Rev. B* **55**, 2938 (1997).
- 524 [36] R. L. C. Vink, G. T. Barkema, and W. F. van der Weg, *Phys. Rev. B* **63**, 115210 (2001).
- 525 [37] I. D. Wolf, *Semicond. Sci. Technol.* **11**, 139 (1996).
- 526 [38] E. Bonera, M. Fanciulli, and D. N. Batchelder, *J. Appl. Phys.* **94**, 2729 (2003).
- 527 [39] D. A. Strubbe, E. C. Johlin, T. R. Kirkpatrick, T. Buonassisi, and J. C. Grossman, *Phys. Rev. B* **92**, 241202(R) (2015).
- 528 [40] B. E. White and R. O. Pohl, *Mater. Res. Soc. Symp. Proc.* **356**, 567 (1995).
- 529 [41] X. Liu and R. O. Pohl, *Phys. Rev. B* **58**, 9067 (1998).
- 530 [42] P. A. Thomas, M. H. Brodsky, D. Kaplan, and D. Lepine, *Phys. Rev. B* **18**, 3059 (1978).
- 531 [43] F. Tuomisto and I. Makkonen, *Rev. Mod. Phys.* **85**, 1583 (2013).
- 532 [44] P. J. Schultz and K. G. Lynn, *Rev. Mod. Phys.* **60**, 701 (1988).
- 533 [45] A. van Veen, H. Schut, M. Clement, J. de Nijs, A. Kruseman, and M. IJpma, *Appl. Surf. Sci.* **85**, 216 (1995).
- 534 [46] P. G. Coleman, *J. Phys.: Conf. Ser.* **265**, 012001 (2011).
- 535 [47] M. Clement, J. M. M. De Nijs, P. Balk, H. Schut, and A. Van Veen, *J. Appl. Phys.* **79**, 9029 (1996).
- 536 [48] R. Brüggemann, P. Reinig, and M. Hölling, *Thin Solid Films* **427**, 358 (2003).
- 537 [49] A. H. M. Smets, W. M. M. Kessels, and M. C. M. van de Sanden, *Appl. Phys. Lett.* **82**, 865 (2003).
- 538 [50] J. A. Floro, P. G. Kotula, S. C. Seel, and D. J. Srolovitz, *Phys. Rev. Lett.* **91**, 096101 (2003).
- 539 [51] R. C. Chittick, *J. Non-Cryst. Solids* **3**, 255 (1970).
- 540 [52] S. C. Moss and J. F. Graczyk, *Phys. Rev. Lett.* **23**, 1167 (1969).
- 541 [53] M. D. Ediger, *J. Chem. Phys.* **147**, 210901 (2017).
- 542 [54] L. Berthier, P. Charbonneau, E. Flenner, and F. Zamponi, *Phys. Rev. Lett.* **119**, 188002 (2017).
- 543 [55] Z. Shi, P. G. Debenedetti, and F. H. Stillinger, *J. Chem. Phys.* **134**, 114524 (2011).
- 544 [56] D. Y. Kim, S. Stefanoski, O. O. Kurakevych, and T. A. Strobel, *Nature Mater.* **14**, 169 (2015).
- 545 [57] D. Beeman and R. Alben, *Adv. Phys.* **26**, 339 (1977).
- 546 [58] G. S. Bales and A. Zangwill, *J. Vac. Sci. Technol. A* **9**, 145 (1991).
- 547 [59] U. v. Hulsén, P. Thiyagarajan, and U. Geyer, *Mater. Res. Soc. Symp. Proc.* **441**, 391 (1996).

- 548 [60] J. A. Floro, S. J. Hearne, J. A. Hunter, P. Kotula, E. Chason, S. C. Seel, and C. V. Thompson, *J. Appl. Phys.* **89**, 4886
549 (2001).
- 550 [61] J. A. Floro, E. Chason, R. C. Cammarata, and D. J. Srolovitz, *MRS Bull.* **27**, 19 (2002).
- 551 [62] J. E. Rowe and H. Ibach, *Phys. Rev. Lett.* **31**, 102 (1973).
- 552 [63] A. Mahan, B. Nelson, S. Salamon, and R. Crandall, *J. Non-Cryst. Solids* **137-138**, 657 (1991).
- 553 [64] E. Guerrero and D. A. Strubbe, *Phys. Rev. Mat.* **4**, 025601 (2020).
- 554 [65] M. Hakala, M. J. Puska, and R. M. Nieminen, *Phys. Rev. B* **57**, 7621 (1998).
- 555 [66] W. Shi, M. Theelen, A. Illiberi, N. Barreau, S. J. van der Sar, M. Butterling, H. Schut, W. Egger, M. Dickmann,
556 C. Hugenschmidt, M. Zeman, E. Brück, and S. W. H. Eijt, *Phys. Rev. Mat.* **2**, 105403 (2018).
- 557 [67] G. A. N. Connell and J. R. Pawlik, *Phys. Rev. B* **13**, 787 (1976).
- 558 [68] J. C. Knights, G. Lucovsky, and R. J. Nemanich, *J. Non-Cryst. Solids* **32**, 393 (1979).
- 559 [69] R. A. Street and D. K. Biegelsen, *Solid State Commun.* **33**, 1159 (1980).
- 560 [70] J. Dabrowski, H. J. Müssig, and G. Wolff, *Phys. Rev. Lett.* **73**, 1660 (1994).
- 561 [71] M. Molina-Ruiz, Y. J. Rosen, H. C. Jacks, M. R. Abernathy, T. H. Metcalf, X. Liu, J. L. DuBois, and F. Hellman, *Phys.*
562 *Rev. Mat.* **5**, 035601 (2021).